

Featuring Semitransparent p–i–n Perovskite Solar Cells for High-Efficiency Four-Terminal/Silicon Tandem Solar Cells

Pei-Huan Lee, Ting-Tzu Wu, Chia-Feng Li, Damian Glowienka, Yu-Xuan Huang, Shih-Han Huang, Yu-Ching Huang,* and Wei-Fang Su*

Two issues need to be resolved when fabricating p–i–n semitransparent perovskite solar cells (ST-PVSCs) for four-terminal (4 T) perovskite/silicon tandem solar cells: 1) damage to the underlying absorber (MAPbI₃), electron transporting layer ([6,6]-phenyl-C₆₁-butyric acid methyl ester, PCBM), and work function (WF) modifier (polyethylenimine, PEI), resulting from the harsh sputtering conditions for the transparent electrodes (TEs) and 2) low average near-infrared transmittance (ANT) of TEs. Herein, a unique SnO₂ layer to protect the MAPbI₃ and PCBM layers is developed and functions as a WF modifier for a new TE (cerium-doped indium oxide, ICO), which exhibits an excellent ANT of 86.7% in the range of 800–1200 nm. Moreover, a MAPbI₃-based p–i–n ST-PVSC is prepared, achieving an excellent power conversion efficiency (PCE) of 17.23%. When it is placed over the Si solar cell, a 4 T tandem solar cell with a PCE of 26.14% is obtained.

1. Introduction

Organic and inorganic perovskite solar cells (PVSCs) are among the most promising emerging photovoltaic technologies for commercialization, due to their inexpensive solution processability and high power conversion efficiencies (PCEs). Recently, the highest certified PCE of a PVSC reached 25.5%, very close to the record PCE of 26.7% for a single-crystalline silicon solar cell (c-Si SC).^[1,2] The PCEs of single-junction solar cells are, however,

limited to 33%, according to theoretical calculations performed using the Shockley–Queisser model.^[3,4] To break through this PCE limitation of single-junction solar cells, it has been proposed to fabricate multijunction solar cells (tandem) from absorbers having different bandgaps. For example, in a two-junction solar cell, the architecture would feature a wide-bandgap solar cell stacked on top of a low-bandgap solar cell. High-energy photons in the solar spectrum would be absorbed by the top cell, producing a high open-circuit voltage (V_{oc}); low-energy photons that are not absorbed by the top cell could be absorbed by the bottom cell. This strategy can significantly minimize both thermalization and absorption losses, thereby increasing the degree of light harvesting and improving the

PCE.^[4,5] Generally, the PCEs of multijunction solar cells are enhanced upon the increasing number of junctions; even in the simplest case of two junctions, the theoretical PCE can be increased from $\approx 33\%$ to 42%.^[6]

Si SCs made from a bandgap of 1.1 eV crystalline silicon have dominated the photovoltaics industry in the past few decades (market share > 90%), due to their adequate efficiency and reliability. In recent years, perovskites have been developed displaying optoelectronic characteristics suitable for highly efficient solar cells, including large optical absorption coefficients, long carrier diffusion lengths, and efficient ambipolar carrier transport.^[7–9] In addition, the bandgaps of perovskite materials can be tuned readily in the range from 1.2 to 2.3 eV through compositional engineering; such tunable bandgaps make these materials very suitable for combining with c-Si SCs to form tandem solar cells.^[10,11] Indeed, perovskite/silicon tandem solar cells have been attracting a great deal of attention from researchers since 2015,^[12–15] with the combination of PVSCs and c-Si SCs as tandem cells easily breaking the PCE limit of single-junction solar cells with only a slight increase in cost.


Two architectures have been used most commonly for perovskite/Si tandem solar cells: mechanically stacked four-terminal (4 T) and monolithic two-terminal (2 T) tandem devices. In the 2 T configuration, the perovskite top cell is deposited on the silicon bottom cell and connected through an interconnection layer; this configuration requires only one transparent electrode (TE). The optical loss from this single TE is much lower than that from the three TEs in the 4 T configuration, which features the top electrode of Si SCs and the rear and front electrodes of

P.-H. Lee, T.-T. Wu, C.-F. Li, S.-H. Huang, W.-F. Su
Department of Materials Science and Engineering
National Taiwan University
Taipei 106, Taiwan
E-mail: suwf@ntu.edu.tw

P.-H. Lee, C.-F. Li, Y.-X. Huang, Y.-C. Huang, W.-F. Su
Department of Materials Engineering
Ming Chi University of Technology
New Taipei 243, Taiwan
E-mail: huangyc@mail.mcut.edu.tw

D. Glowienka
Faculty of Applied Physics and Mathematics
Gdańsk University of Technology
Gdańsk 80-233, Poland

S.-H. Huang
FrontMaterials Corporation Ltd.
Taipei 10087, Taiwan

 The ORCID identification number(s) for the author(s) of this article can be found under <https://doi.org/10.1002/solr.202100891>.

DOI: 10.1002/solr.202100891

semitransparent perovskite solar cells (ST-PVSCs). Thus, the 2 T configuration is generally expected to provide a PCE higher than that from the 4 T configuration. It remains challenging, however, to uniformly place a perovskite layer on top of the textured structure of Si SCs.^[16,17] In addition, it is necessary to ensure photocurrent matching between these two cells, because the photocurrent of a 2 T tandem cell is limited by that of the subcell having the lower current.^[18] Therefore, the bandgap of the perovskite top cell is an important parameter when optimizing the PCE of a 2 T tandem cell. In contrast, in the 4 T configuration, the perovskite top cell and the silicon bottom cell are fabricated independently and stacked together mechanically. Both cells are fabricated under their individually optimal conditions. Moreover, each of the two subcells is connected to its own tracking system, so there is no need for photocurrent matching between the two subcells of the 4 T tandem device. Furthermore, because there is a considerable difference in stability between PVSC and Si SCs, the 4 T configuration has another advantage in that it is possible to simply replace sp PVSCs.

When developing a 4 T perovskite/silicon tandem cell, both the rear and front electrodes of the PVSCs must be transparent, functioning as semi-transparent PVSCs (ST-PVSCs). Many types of TEs have been applied to fabricate ST-PVSCs, including ultrathin metal films,^[19,20] metal nanowires,^[21,22] carbon nanotubes,^[23,24] conducting polymers,^[25,26] and transparent conductive oxides (TCOs).^[27–29] Among them, TCOs are preferred because of their high transmittance, excellent chemical stability, high conductivity, and long-term durability. TCO thin films are usually manufactured using sputtering processes. The following issues must be overcome, however, when manufacturing ST-PVSCs using sputtered TCO films. First, the deposition of energetic ions through sputtering can damage the soft materials beneath the rear TCO of a p–i–n device, namely, the work function (WF) modifier (polyethylenimine, PEI), the electron transport layer ([6,6]-phenyl-C₆₁-butyric acid methyl ester, PCBM), and the light absorption layer (the perovskite MAPbI₃). To protect the underlying layers, it is necessary to use a buffer layer having good optoelectronic properties; a durable SnO₂ layer is a good candidate for p–i–n devices. However, most SnO₂ layers have been prepared using atomic layer deposition,^[30–34] which is complex and costly for mass production. Therefore, solution-processable SnO₂ buffer layers are highly desirable. Second, commercially available TEs (typically fluorine-doped tin oxide [FTO] and indium tin oxide [ITO]) have been used widely in the fabrication of ST-SCs, but usually they must be highly doped to achieve high conductivity. According to the Drude–Lorentz model, highly doped TCO electrodes suffer from free carrier absorption (FCA) in the near-infrared (NIR) range, caused by plasma oscillation and proportional to the free carrier density.^[35,36] The FCA effect induces a parasitic absorption in the NIR region, thereby decreasing the average NIR transmittance (ANT) of ST-PVSCs. Although minimizing the free carrier density of the TCO is an effective means of eliminating the FCA,^[36] the lower number of free carriers would also lower the conductivity (σ) of the TCO film, following the equation

$$\sigma = e\mu N_e \quad (1)$$

where e is charge per carrier, N_e is the carrier density, and μ is the carrier mobility. Therefore, a tradeoff exists between high conductivity and a low FCA. Although many alternative TCO materials have been reported, there remains room for improving their performance. Sputtered Zn-doped In₂O₃ (IZO) exhibits a mobility of 50–60 cm² V⁻¹ s⁻¹,^[28,37] but it features a parasitic absorption in the ultraviolet region because of its amorphous nature. Although Zr-doped indium oxide (IZRO) TEs exhibit good carrier mobility (≈ 77 cm² V⁻¹ s⁻¹),^[29] it is less than that of the high-conductivity metal oxide (> 100 cm² V⁻¹ s⁻¹). The carrier mobility of hydrogen-doped In₂O₃ (IO:H) exceeds 100 cm² V⁻¹ s⁻¹,^[38] but its preparation includes the introduction of water vapor during sputtering deposition. Precisely controlling the minute amounts of water vapor between batches can be challenging, potentially resulting in poor film quality. Furthermore, thermally induced diffusion of H₂ can make these films unstable at high temperature.^[39] Recently, cerium-doped indium oxide (ICO) has been used as the electrode material in silicon heterojunction (SHJ) solar cells because of its high carrier mobility and NIR transparency.^[40] Therefore, it would appear to be a good candidate also for use as the TE material in ST-PVSCs.

In this study, we fabricated ST-PVSCs having the p–i–n structure TCO/NiO_x/MAPbI₃/PCBM/buffer layer/TCO. We synthesized unique SnO₂ nanoparticles for use as the buffer layer, prepared through an inexpensive solution-coating process. This buffer layer performed dual functions: protecting the PCBM and perovskite layers from sputtering damage and tuning the WF to match the energy levels of PCBM and TCO without using PEI. We systematically varied the processing conditions of the ICO to achieve a high carrier mobility, a low free carrier density, and high NIR transmittance for both the front and rear TCO electrodes. Furthermore, we fabricated a MAPbI₃-based p–i–n ST-PVSC, having an outstanding PCE of 17.23% and an ANT of 76.8% (Table S1 and Figure S1, Supporting Information). When we placed this ST-PVSC on top of a heterojunction (HJT) c-Si SC (23% PCE), we obtained a 4 T tandem device displaying a PCE of 26.14%.

2. Results and Discussion

Throughout this study, we used devices having the p–i–n configuration front TCO/hole transport layer (HTL)/absorber/electron transport layer (ETL)/buffer layer/rear TCO because of its good device stability.^[41] Here, the HTL was NiO_x, the absorber was MAPbI₃, the ETL was PCBM, and the buffer layer was a film of tetrabutylammonium hydroxide-capped SnO₂ (TBAOH-SnO₂). The TCO was ITO, FTO, or ICO. The results of our systematic study of the buffer layer and TCO for the fabrication of ST-PVSCs are discussed, along with the use of these ST-PVSCs in perovskite/Si 4T tandem solar cells.

2.1. Fabrication of Semitransparent PVSCs Using Solution-Processable TBAOH-SnO₂ Buffer Layer

A robust metal oxide should be used as the buffer layer material to protect the underlying soft materials (PEI, PCBM, and MAPbI₃) of p–i–n devices during the sputtering of the TCO electrode when preparing semitransparent devices. SnO₂ is an

n-type semiconductor material, suitable for depositing on top of the PCBM layer to facilitate electron transport in the device. In our previous study, we found that a film of TBAOH–SnO₂ can perform dual functions: a durable n-type electron transport material and a WF modifier for the metal electrode.^[42] In this present study, we used TBAOH–SnO₂ as the buffer layer of the sputtered TCO electrode and found that TBAOH also exhibits the WF modification effect on the TCO electrode. The ITO rear electrode was the first TCO to be evaluated. Through simple spin coating, the TBAOH–SnO₂ film was deposited on top of the PCBM layer. Therefore, the TBAOH ligand, which capped around the SnO₂ nanoparticles, can form the molecular dipole-induced electrical field at the SnO₂–ITO interface, thereby modifying the WF of ITO. **Figure 1a** displays the molecular dipole of TBAOH, determined using ultraviolet photoelectron spectroscopy (UPS), revealing a WF shift of ITO from –4.67 to –3.69 eV. Thus, an ohmic contact was formed at the interface between TBAOH–SnO₂ and ITO to achieve efficient electron extraction, as illustrated in Figure 1b. The optimal sputtering conditions of ITO (50 W direct current [DC] power under 3 mtorr of Ar) were determined by varying the pressure of Ar atmosphere and varying the DC power from 30 to 90 W. Figure S2, Supporting Information, reveals that the TBAOH–SnO₂ layer functioned well when the DC power reached up to 50 W, but the fill factor (FF) and open-circuit voltage (*V*_{oc}) of the ST-PVSC decreased greatly, as a result of destruction of the buffer layer, when the DC power was greater than 50 W. Figure 1c displays the device structure and cross-sectional

scanning electron microscopy (SEM) image of the ST-PVSC. To demonstrate the dual functions of the TBAOH–SnO₂ layer for the sputtered ITO, for comparison, we fabricated ST-PVSCs containing PEI as the organic WF modifier. Table S2, Supporting Information, summarizes the data from the *J*–*V* curves of the opaque PVSCs and ST-PVSCs incorporating the PEI and TBAOH–SnO₂ layers. Both the opaque PVSCs provided high efficiencies (>18%), indicating that the PEI and TBAOH–SnO₂ layers were both effective as WF modifiers. Nevertheless, the ST-PVSC incorporating PEI provided a low PCE (1%) and a low FF (38%), consistent with the sputtered ITO damaging the soft material layers. In contrast, the ST-PVSC incorporating TBAOH–SnO₂ provided a good PCE (16.53%) and FF (75%) and exhibited negligible hysteresis (Figure S3, Supporting Information). Thus, the TBAOH–SnO₂ layer protected the underlying materials during the sputter deposition process. To confirm that the TBAOH–SnO₂ layer could function as a WF modifier, we also tested the effects of pristine SnO₂ (i.e., without TBAOH capping) as a buffer layer in the ST-PVSC; Figure S4, Supporting Information, presents its *J*–*V* curve. Interestingly, although the pristine SnO₂ layer protected the soft materials from damage during the sputtering process, the *J*–*V* curve of the ST-PVSC featured an s-shaped kick, implying that charges accumulated at the SnO₂–ITO interface as a result of energy misalignment between the SnO₂ and ITO layers. Moreover, we performed electrical modeling to investigate the effect of the TCO sputtering process on device performance. We used drift-diffusion modeling on

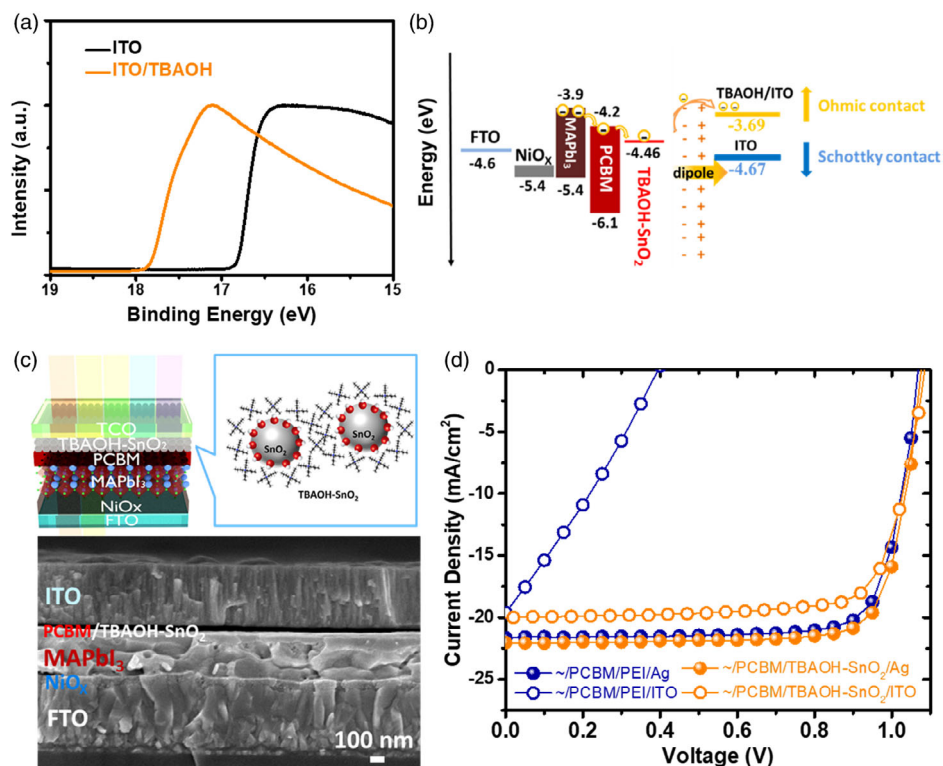


Figure 1. a) UPS spectra of ITO and TBAOH-modified ITO. b) Energy band diagram of ST-PVSCs prepared with and without TBAOH-SnO₂. c) Schematic representation and cross-sectional SEM image of an ST-PVSC. d) *J*–*V* curves of opaque PVSCs and ST-PVSCs fabricated from PCBM/PEI and PCBM/TBAOH-SnO₂.

both the front and rear sides of the ST-PVSCs. The experimental data were in good agreement with the simulations, with a value of R^2 of 98.7% (Figures S5, Supporting Information). The R^2 corresponds to goodness of fit from the regression analysis, and the value is in the range of 0–100%, depending on how well the experimental results match simulated data. Front-side illumination led to a higher PCE, because the front electrode featured lower parasitic optical absorption. Table S3, Supporting Information, lists the fitting parameters extracted from modeling. Notably, even when the sputtered TCO was deposited on the ETL side, the defect density at the perovskite–ETL interface was half of that at the HTL–perovskite interface. Thus, TBAOH–SnO₂ provided very good protection and tunability of the WF of the sputtered TCO electrode and confirmed the suitability of this unique dual-function TBAOH–SnO₂ layer for the manufacture of ST-PVSCs.

2.2. Development of Highly NIR-Transparent Cerium-Doped Indium Oxide

We have successfully fabricated ST-PVSCs featuring ITO as the rear electrode and FTO as the front electrode. Nevertheless, both FTO and ITO suffer from low-NIR transmittance (at wavelengths ranging from 800 to 1200 nm) because of their high carrier densities. In this study, we replaced both of these TCO electrodes with 3 wt% cerium-doped indium oxide (ICO). The ionic radius of tetravalent cerium (87 pm) is very close to that of trivalent indium (80 pm), thereby minimizing lattice distortion near the dopant site. Therefore, the carrier mobility of ICO can be improved and its ANT can be maintained without heavy doping. The processing conditions for the rear electrode (r-ICO) were different from those for the front electrode (f-ICO), due to the difference in the materials underlying these ICOs. We discuss them separately, as follows.

For the preparation of the rear electrode, the ICO was deposited directly on top of the soft layers of the device. Therefore, we could not use a high sputter power or thermal annealing. We chose to use DC power, instead of radio-frequency (RF) power, because it provided a higher deposition rate and less of a thermal effect at a fixed power (Figure S6, Supporting Information). Nevertheless, DC sputtering leads to the issue of positive charge accumulation on the target surface, inducing a change in the film composition and generating oxygen vacancies in the TCO film.^[43,44] Although oxygen vacancies are required to ensure a high free carrier density, free carriers are strongly absorbed in the NIR region, resulting in low-NIR transmittance. Therefore, we attempted to minimize the oxygen vacancies through passivation, by introducing a flow of oxygen during the sputtering process. The optimal oxygen flow rate was determined by varying the ratio of oxygen [$r(\text{O}_2) = \text{O}_2/(\text{Ar} + \text{O}_2)$] under a working pressure of 3 mtorr at a fixed film thickness of 300 nm. We used X-ray photoelectron spectroscopy (XPS), Hall effect measurements, and UV–vis–NIR spectroscopy to characterize the ICO films in terms of their chemical compositions and chemical states, electronic properties, and optical properties, respectively. Figure 2 and Table 1 summarize the results. The chemical binding energies of In 3d_{5/2} and In 3d_{3/2} were located at 443.55 and 451.15 eV, respectively

(Figure S7a, Supporting Information). The two peaks in the Ce 3d XPS spectrum were resolved into five Gaussian curves representing Ce⁴⁺ and Ce³⁺ oxidation states.^[45] The signals of Ce⁴⁺ were very strong, indicating that Ce⁴⁺ ions could replace In³⁺ ions in the lattice and generate free carriers (Figure S7b, Supporting Information). The O 1s XPS spectrum was resolved into three Gaussian components, with binding energies of 529.00, 530.55, and 531.45 eV, respectively (Figure S7c, Supporting Information). The peak with the lowest binding energy at 529.00 eV represents the bonded oxygen ions (O_I) adjacent to In atoms in the complete In₂O₃ lattice. The peak at 530.55 eV represents the O²⁻ ions near the oxygen-deficient region in the In₂O₃ lattice (O_{II}); it can be related to oxygen vacancies. The peak at 531.45 eV represents the interstitial oxygen ions in the In₂O₃ lattice or the OH groups on the surface (O_{III}). Figure 2a reveals the effect of the oxygen flow ratio on the composition of O 1s in the r-ICO film. As the value of $r(\text{O}_2)$ increased from 0 to 0.27%, the ratio of oxygen-deficient regions to total oxygen (O_{II}/O_{total}) decreased from 36.21% to 34.30%. Thus, by introducing oxygen during the sputter-deposition process, the amount of oxygen vacancies could be minimized effectively through oxygen passivation.^[46,47] Furthermore, we observed that when the value of $r(\text{O}_2)$ increased to 0.27%, the ratio of interstitial oxygen to total oxygen (O_{III}/O_{total}) increased to 23.4% because of the presence of oxygen ions in the lattice.^[48,49] Figure 2b reveals that the free carrier density (N_e) of the ICO decreased upon increasing the value of $r(\text{O}_2)$, thereby improving the ANT of the ICO film. When the value of $r(\text{O}_2)$ reached 0.13%, the mobility (μ) of the film increased as a result of the passivation of oxygen vacancies, as described earlier. When we increased the value of $r(\text{O}_2)$ further to 0.27%, interstitial oxygen that formed also acted as a scattering factor and decreased the carrier mobility. In short, applying an optimal value of $r(\text{O}_2)$ of 0.13% provided the r-ICO with a lower sheet resistance (28.75 Ωsq^{-1} ; $N_e = 2.34 \times 10^{20} \text{cm}^{-3}$; $\mu_e = 32.51 \text{cm}^2 \text{V}^{-1} \text{s}^{-1}$) and higher ANT (80%) than those of the other r-ITO samples. Accordingly, we used this ICO as the rear electrode for ST-PVSCs prepared throughout the remainder of this study.

Because the f-ICO electrode was prepared on a glass substrate, there were no strict limitations on its sputtering power or processing temperature. Therefore, we chose RF sputtering to prepare the f-ICO, because it occurs with fewer composition variations (Figure S7, Supporting Information) and provides better film quality (Figure S8, Supporting Information) when compared with DC sputtering. We obtained the 300 nm f-ICO film by applying a high power of 240 W under Ar atmosphere with a working pressure of 3 mtorr. To improve the film quality after sputtering, we performed annealing at various temperatures. We used X-ray diffraction (XRD), SEM, and XPS to evaluate the film characteristics. The as-deposited f-ICO film exhibited a broad XRD diffraction signal (Figure 3a), implying that it was amorphous. The crystallinity of the f-ICO film improved upon increasing the annealing temperature. For the f-ICO film annealed at 400 °C, the (222) diffraction peak appeared at a high diffraction angle, indicating that its lattice was denser than those of the f-ICO films annealed at lower temperatures. This high annealing temperature promoted the rearrangement of atoms by adjusting the lattice alignment and minimizing defects, thereby forming denser crystals. The SEM image of the f-ICO

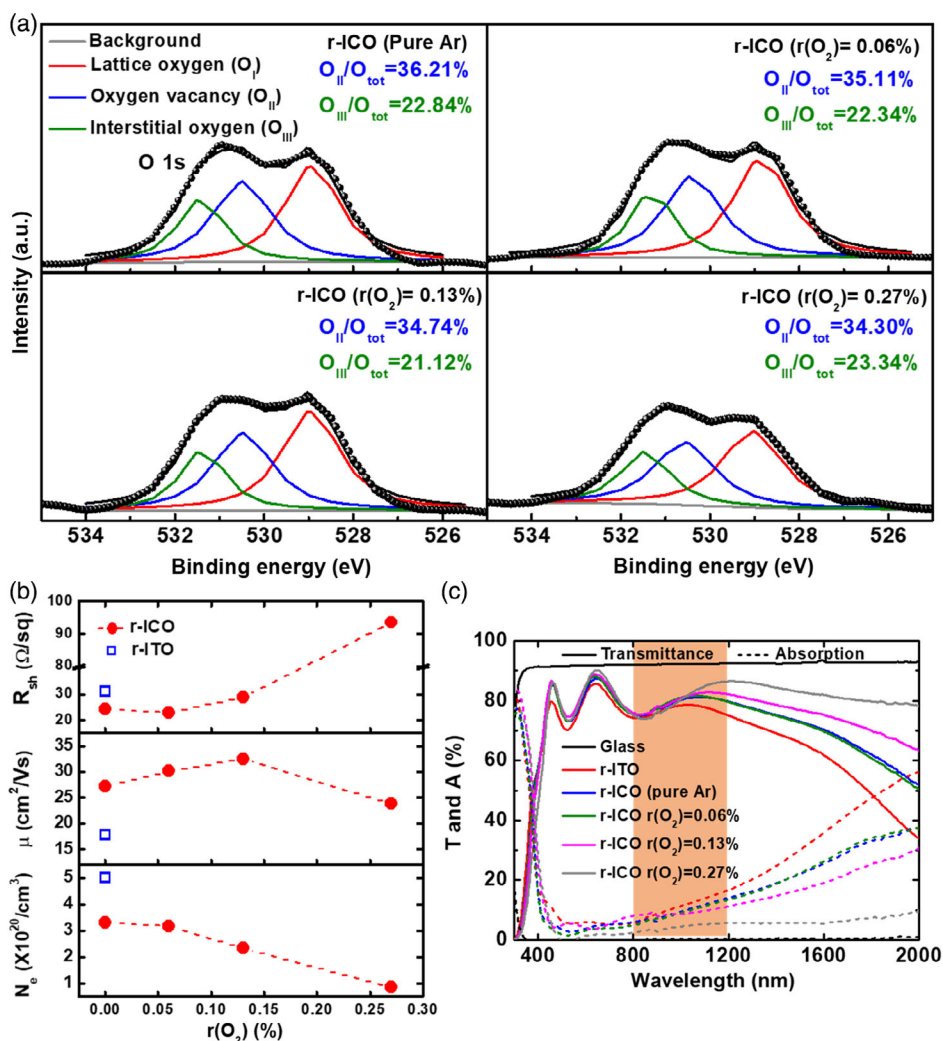


Figure 2. a) O 1s XPS spectra, b) sheet resistances, carrier mobilities, and free carrier densities, and c) UV-vis-NIR transmittance and absorption spectra of r-ICO electrodes prepared under various oxygen flow ratios during sputter deposition.

Table 1. Effect of the value of $r(\text{O}_2)$ on the sheet resistance, carrier mobility, free carrier density, and ANT of r-ICO electrodes.

Rear electrode	Oxygen fraction, $r(\text{O}_2)$ [%]	Sheet resistance, R_{sh} [$\Omega \text{ sq}^{-1}$]	Carrier mobility, μ [$\text{cm}^2 \text{ V}^{-1} \text{ s}^{-1}$]	Free carrier density, N_e [$\times 10^{20} \text{ cm}^{-3}$]	ANT (800–1200 nm) [%]
r-ITO	0	31.28 ± 1.21	17.77	5.02	76.77
r-ICO	0	24.11 ± 0.51	27.13	3.31	79.02
	0.06	22.98 ± 0.57	30.14	3.17	79.37
	0.13	28.75 ± 0.94	32.51	2.34	80.00
	0.27	93.51 ± 10.82	23.80	0.85	80.24

film annealed at 200 °C revealed that new crystal grains formed and were distributed in the amorphous matrix; when the annealing temperature was increased to 400 °C, the crystals shrank slightly to cause a larger grain boundary and a denser film, consistent with the XRD analyses. The XPS pattern of the as-deposited ICO film prepared through RF sputtering was different from that of the aforementioned DC-sputtered film

(Figure S7, Supporting Information). Figure S9, Supporting Information, presents the O 1s XPS spectra of the f-ICO films annealed at various temperatures. Upon increasing the annealing temperature from room temperature to 400 °C, the $\text{O}_{\text{II}}/\text{O}_{\text{tot}}$ ratio decreased accordingly from 33.62 to 24.33%, indicating that the content of oxygen vacancies also decreased accordingly. Table 2 and Figure 3c summarize the electrical

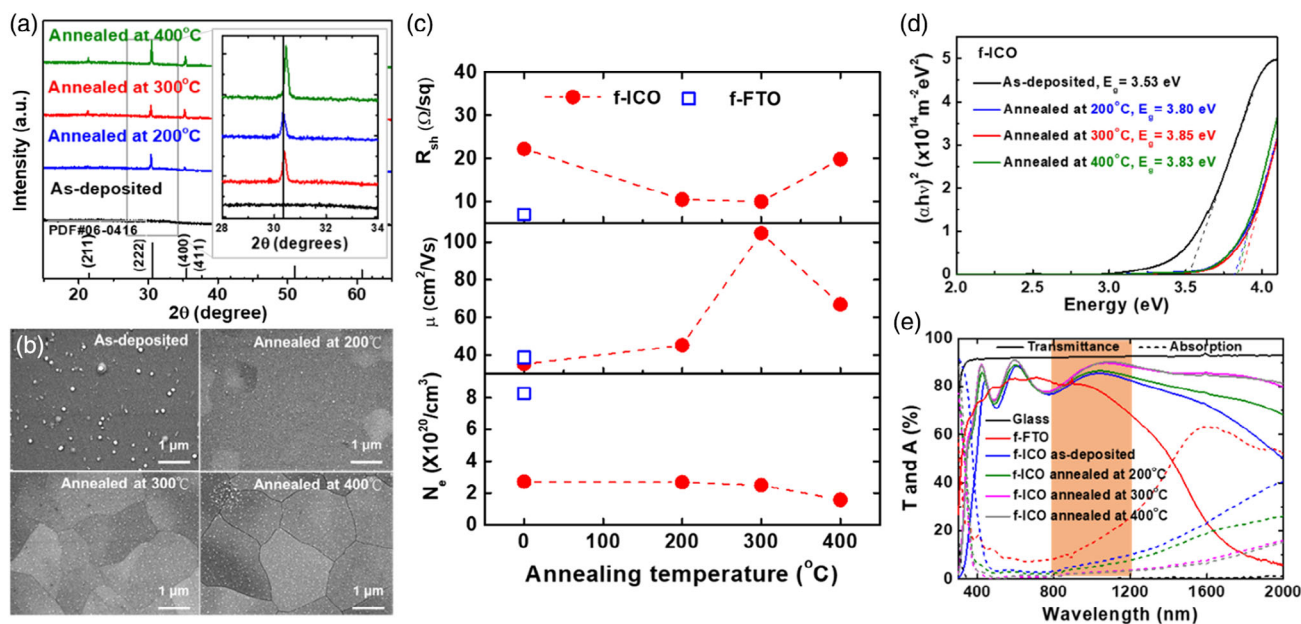


Figure 3. a) XRD patterns (whole view and enlarged view of the (2 2 2) peak), b) SEM top-view images, c) sheet resistances, carrier mobilities, and free carrier densities, d) optical bandgaps (E_g) calculated using the Tauc plot method, and e) UV-vis-NIR transmission and absorption spectra of f-ICO electrodes annealed under vacuum at various annealing temperatures.

Table 2. Effect of annealing temperature on the sheet resistance, carrier mobility, free carrier density, AVT, and ANT of f-ICO electrodes.

Front electrode	Annealing temperature [°C]	Sheet resistance, R_{sh} [$\Omega \text{ sq}^{-1}$]	Carrier mobility, μ [$\text{cm}^2 \text{ V}^{-1} \text{ s}^{-1}$]	Free carrier density, N_e [$\times 10^{20} \text{ cm}^{-3}$]	AVT (400–800 nm) [%]	ANT (800–1200 nm) [%]
f-FTO	–	≈ 7	38.62	8.27	81.02	77.69
f-ICO	(As deposited)	22.20 ± 1.54	32.55	3.13	79.11	82.94
	200	10.74 ± 0.68	82.21	2.56	80.87	84.02
	300	9.99 ± 0.94	104.70	2.49	82.45	86.72
	400	19.81 ± 3.92	70.79	1.91	82.18	86.65

properties of the f-ICO films annealed at various temperatures. Upon increasing the annealing temperature, the free carrier density decreased because of a decrease in the number of oxygen vacancies, as discussed earlier for the DC-sputtered films. Interestingly, the carrier mobility increased initially and then decreased upon increasing the annealing temperature. Because an ordered structure provides less of a scattering effect, it is known that the carrier mobility will increase upon improving the crystallinity. In addition to the crystallinity, the mobility is also determined by the grain boundary scattering effect. The grain boundary of the f-ICO film annealed at 400 °C was coarse, as revealed in its SEM image (Figure 3b), thereby intensifying the grain boundary scattering effect and decreasing the carrier mobility. Thus, the film annealed at 300 °C exhibited the best conductivity. Figure 3d presents the optical bandgaps of the annealed films. The bandgap of the f-ICO film increased upon increasing the annealing temperature, due to improved film crystallinity. Therefore, the optical absorption in the ICO film underwent a blueshift, significantly increasing the average visible light transmittance (AVT). Figure 3e displays the ANTs of the ICO films annealed at the various temperatures. The ANT of the

as-deposited ICO film (82.94%) increased to 86.72% after annealing at 300 °C but decreased slightly to 86.65% after annealing at 400 °C. The improvement in ANT was due to the decrease in free carrier density. Compared with the commercial f-FTO, each of our f-ICO films in this study featured a lower carrier density, a higher mobility, and a higher ANT. The f-ICO film annealed at 300 °C exhibited the best performance: a low sheet resistance of $9.99 \Omega \text{ sq}^{-1}$ ($N_e = 2.49 \times 10^{20} \text{ cm}^{-3}$; $\mu_e = 104.7 \text{ cm}^2 \text{ V}^{-1} \text{ s}^{-1}$), a high AVT of 82.45%, and an ANT of 86.72%. Therefore, we used the f-ICO film annealed at 300 °C as the front electrode of ST-PVSCs for the fabrication of perovskite/silicon tandem cells.

2.3. Highly NIR-Transparent PVSCs and 4T Perovskite/silicon Tandem Solar Cells

We investigated the effects of the various TCOs on the performance of ST-PVSCs (Figure 4 and Table 3). The devices denoted “f-FTO/r-ITO” and “f-ICO/r-ICO” were fabricated from combinations of f-FTO/r-ITO and f-ICO/r-ICO electrodes,

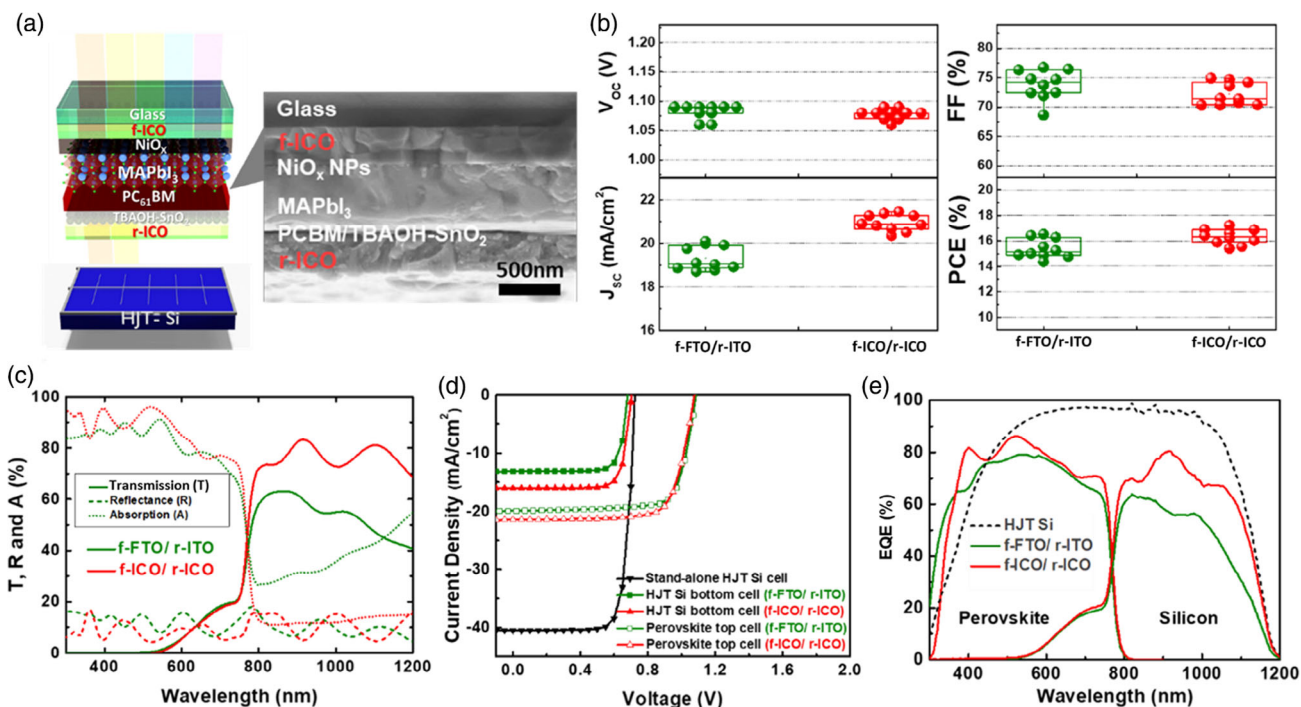


Figure 4. a) Schematic representation of a 4 T perovskite/silicon tandem solar cell and cross-sectional SEM image of an ST-PVSC fabricated using f-ICO/r-ICO electrodes. b) Distribution of photovoltaic parameters, c) UV-vis-NIR transmission, reflection, and absorption spectra of ST-PVSCs with f-FTO/r-ITO and f-ICO/r-ICO electrodes. d) J - V curves and e) EQE spectra of a standalone HJT Si SC, perovskite top cells with various combinations of electrodes, and HJT silicon bottom cells.

Table 3. Device performance of perovskite top cells with various combinations of electrodes, a standalone HJT si SC, HJT silicon bottom cells, and 4T perovskite/silicon tandem solar cells. Average data obtained from at least 12 devices. Photovoltaic parameters of the champion cell are provided in parentheses.

Device	V_{oc} [V]	J_{sc} [mA cm^{-2}]	FF [%]	PCE [%]
Perovskite top cell	1.09 ± 0.01	19.54 ± 0.57	74.59 ± 2.79	15.83 ± 0.63
f-FTO/r-ITO	(1.09)	(19.92)	(76.44)	(16.53)
Perovskite top cell	1.08 ± 0.01	20.93 ± 0.42	73.63 ± 1.50	16.64 ± 0.57
f-ICO/r-ICO	(1.08)	(21.44)	(74.66)	(17.23)
Standalone HJT Si cell	0.72 ± 0.01	40.12 ± 0.33	78.81 ± 0.37	22.68 ± 0.31
	(0.72)	(40.50)	(78.79)	(23.07)
HJT Si bottom cell	0.68 ± 0.01	12.82 ± 0.15	78.19 ± 0.53	6.85 ± 0.10
f-FTO/r-ITO	(0.68)	(13.13)	(78.30)	(7.00)
HJT Si bottom cell	0.70 ± 0.00	15.72 ± 0.05	78.91 ± 0.15	8.69 ± 0.04
f-ICO/r-ICO	(0.70)	(16.00)	(79.46)	(8.90)
4 T tandem solar cell	—	—	—	22.83 ± 0.63
f-FTO/r-ITO				(23.53)
4 T tandem solar cell	—	—	—	25.56 ± 0.57
f-ICO/r-ICO				(26.14)

respectively. Figure 4a displays a schematic representation of the tandem solar cells and a cross-sectional SEM image of the ST-PVSC fabricated from the f-ICO and r-ICO electrodes. The PCE of the f-FTO/r-ITO device (16.5%) was lower than that of the f-ICO/r-ICO device (17.2%), resulting from the AVT of f-ICO (82.5%) being higher than that of f-FTO (81%). In addition,

we found that the ST-PVSCs with f-ICO/r-ICO showed a higher series resistance (R_s) ($5.51 \Omega \text{ cm}^2$) than the devices with f-FTO/r-ITO ($5.01 \Omega \text{ cm}^2$), resulting in the lower FF. As all the devices have the same ETL, perovskite, and HTL, the main affecting factor for R_s should be the resistance of the TEs. Therefore, the FF of the f-ICO/r-ICO device was lower than that of the f-FTO/r-ITO

device, due to the sheet resistance of f-ICO ($\approx 10 \Omega \text{sq}^{-1}$) being higher than that of f-FTO ($\approx 7 \Omega \text{sq}^{-1}$). Figure 4b reveals the low variation in the photovoltaic performance of the different batches of ST-PVSCs, indicating the good reproducibility of the device fabrication process. We used UV-vis-NIR spectroscopy to explore the influence of the different TCOs on the ANT of the ST-PVSCs (Figure 4c). The ANT of the ST-PVSC improved from 53.73% to 76.74% after replacing the electrode combination from f-FTO/r-ITO to f-ICO/r-ICO, mainly due to the lower FCAs of both the f-ICO and r-ICO electrodes. Thus, more NIR light could pass through the perovskite top cell and be used by the silicon bottom cell, thereby improving the performance of the perovskite/silicon tandem solar cells.

We stacked the ST-PVSC mechanically on top of the silicon bottom cell to fabricate 4T perovskite/silicon tandem solar cells. Because the perovskite top cell mainly absorbed visible light, it functioned as a filter for the HJT c-Si SC, with only NIR light being absorbed by the HJT c-Si bottom cell. Table 3 and Figure 4d summarize the performance and J - V curves of the standalone HJT c-Si SCs, perovskite top cell, and filtered HJT c-Si bottom cells. The PCE of the standalone HJT c-Si SC was $\approx 23\%$, with a short-circuit current density (J_{sc}) of 40.5 mA cm^{-2} , a value of V_{oc} of 0.72 V, and FF of 78.79%. The HJT c-Si bottom cells filtered by the ST-PVSCs having f-FTO/r-ITO and f-ICO/r-ICO electrodes provided values of J_{sc} of 13.13 and 16.00 mA cm^{-2} , respectively. This improvement in short-circuit current density arose from the ANT of the f-ICO/r-ICO device being higher than that of the f-FTO/r-ITO device, as we discussed in the previous section. Accordingly, the PCEs of the HJT c-Si bottom cells filtered by ST-PVSCs having f-FTO/r-ITO and f-ICO/r-ICO electrodes were 7.00% and 8.90%, respectively. Figure 4e presents the external quantum efficiency (EQE) spectra of the various ST-PVSCs, standalone HJT c-Si SCs, and filtered HJT c-Si bottom cell. The integrated value of J_{sc} from the EQE spectrum of each cell was consistent with the value measured from its J - V curve. As a result, the PCEs of the 4T perovskite/silicon tandem cells with ST-PVSCs fabricated using f-FTO/r-ITO and f-ICO/r-ICO electrodes were 23.53% and 26.14%, respectively. The PCEs of all the tandem devices were higher than that of the standalone HJT c-Si SC. By replacing the electrode combination from f-FTO/r-ITO to f-ICO/r-ICO, the PCEs of the perovskite top cell and silicon bottom cell increased by 0.7 and 1.90%, respectively. Thus, the PCE of the mechanically stacked 4T perovskite/silicon tandem solar cell reached 26.14%. In summary, ICO is a very good TE material for ST-PVSCs when fabricating tandem solar cells with Si solar cells.

3. Conclusion

We have fabricated highly efficient ST-PVSCs having the p-i-n structure TCO/NiO_x/MAPbI₃/PCBM/buffer layer/TCO. We synthesized unique SnO₂ nanoparticles to fabricate the buffer layer using an inexpensive solution-coating process. Use of this new buffer layer avoided damage to the underlying soft materials during the sputter processing of the TCO. The buffer layer not only protected the soft materials PCBM and MAPbI₃ but also tuned the WF of the TCO in line with that of the ETL, without the need for PEI. We systematically investigated the optimal

processing conditions to obtain ICO as a new type of TCO. This ICO exhibited high carrier mobility, a low free carrier density, and a high NIR transmittance suitable for the fabrication of ST-PVSCs. The r-ICO was used to replace ITO, processed through DC sputtering with a low thermal effect; it displayed a carrier mobility of $32.51 \text{ cm}^2 \text{V}^{-1} \text{s}^{-1}$, a free carrier density of $2.34 \times 10^{20} \text{ cm}^{-3}$, a sheet resistance of $28.75 \Omega \text{sq}^{-1}$, and an ANT of 80%. The f-ICO, used to replace FTO, was processed through RF sputtering and annealed at 300 °C to improve its performance; it displayed a carrier mobility of $104.7 \text{ cm}^2 \text{V}^{-1} \text{s}^{-1}$, a free carrier density of $2.49 \times 10^{20} \text{ cm}^{-3}$, a sheet resistance of $9.99 \Omega \text{sq}^{-1}$, and an ANT of 86.72%. When we used ICO for both the front and rear electrodes, the ANT of device increased significantly, from 53.73% to 76.74%, thereby enhancing the PCE of the 4T p-i-n perovskite/silicon tandem cell from 23.53% to 26.14%. Furthermore, the development of the TBAOH-SnO₂ buffer layer and ICO electrodes in this study has potential for application also for the fabrication of high-performance 2T perovskite/silicon tandem cells.

4. Experimental Section

Materials: Chlorobenzene (CB, >99.0%), *N,N*-dimethylformamide (DMF, 99.8%), dimethyl sulfoxide (DMSO, >99.9%), and isopropyl alcohol (IPA, 99.8%) were purchased from Acros Organics. Diethyl ether (99.0%) and ethyl alcohol (EtOH 99.99%) were purchased from Fisher Chemical. PEI (branched; $M_w = \approx 25\,000$) was purchased from Alfa Aesar. FTO glasses, 97 wt% In₂O₃ and 3 wt% CeO₂ sputter target (ICO), 90 wt% In₂O₃ and 10 wt% SnO₂ (ITO), methylammonium iodide (MAI), lead iodide (PbI₂, 99.9985%), and PC₆₁BM (99.0%) were purchased from FrontMaterials. Glass substrates (Corning Eagle XG) were purchased from Corning.

Preparation of TBAOH-SnO₂ Solution: SnO₂ NPs were synthesized using a solvothermal method. The precursor solution was prepared by adding SnCl₄ (3.12 g, 0.012 mol) to a mixed solvent of benzyl alcohol and toluene (3:1, v/v; 20 mL). This precursor solution was transferred to a 25-mL Teflon-lined autoclave and heated at 180 °C for 12 h in an oven. The white precipitate was collected by centrifugation and washed once with diethyl ether and twice with EtOH. To prepare the oleic acid (OA)-SnO₂ suspension, the collected SnO₂ NPs were redispersed in CHCl₃ (5 mL), and OA (1 mL) was added to form a milky suspension. During ultrasonication, butylamine (BA, 1 mL) was added to obtain a colorless transparent suspension. OA-SnO₂ suspension was purified by adding acetone to wash out excess OA and BA, followed by centrifugation and re-dispersion in CHCl₃ at a concentration of 200 mg mL⁻¹. To remove any OA molecules attached to the surface of the SnO₂ NPs, the OA-SnO₂ nanoparticle (NP) suspension (50 μL) was added into a solution of 8 mM boron trifluoride etherate (BF₃-OEt₂) in CH₂Cl₂ (3 mL). The SnO₂ NPs that precipitated immediately were collected by centrifugation. To obtain the TBAOH-capped SnO₂ NP suspension, the collected SnO₂ NPs were added into a solution containing TBAOH (30 mg) and EtOH (1 mL) and then subjected to ultrasonication for several minutes, giving a colorless suspension. The TBAOH-SnO₂ NPs were precipitated by adding hexane to wash out the excess TBAOH. The precipitated SnO₂ NPs were redispersed in EtOH. The TBAOH-SnO₂ NP suspension at a concentration of 10 mg mL⁻¹ was a well-dispersed, stable, and clear solution.

Deposition of the Rear ITO Electrode: A target material comprising 90 wt % In₂O₃ and 10 wt% SnO₂ (SnO₂:In₂O₃, ITO, FrontMaterials) was used to prepare the ITO rear electrode (r-ITO). The samples were transferred into the chamber of a sputtering machine; the chamber was evacuated until the pressure was less than 2×10^{-6} torr, to eliminate the excess oxygen and moisture. (Note: To confirm their electrical and optical properties, the r-ITO films were deposited on soda lime glass [Corning Eagle XG.]). Pure Ar was used as the processing gas. To prevent destruction of the

perovskite layer and the PC₆₁BM ETL from high-energy particles and high-temperature environments, the r-ITO electrode was deposited through DC sputtering (Kao Duen Tec. Co.) with a low sputter power of 50 W under a working pressure of 3 mtorr.

Deposition of the Rear ICO Electrode: A target material with 97 wt% In₂O₃ and 3 wt% CeO₂ (CeO₂:In₂O₃, ICO, FrontMaterials) was used to prepare the ICO rear electrode (r-ICO). The samples were transferred into the chamber of a sputtering machine; the chamber was evacuated until the pressure was less than 2×10^{-6} torr, to eliminate excess oxygen and moisture. Pure Ar and an O₂/Ar (1:99, v/v) gas mixture were used as processing gases. r-ICO electrode was deposited through DC sputtering (Kao Duen Tec. Co.) with the same conditions as those used for ITO sputtering. Atmospheres with different oxygen flow to total flow ratios [$r(\text{O}_2) = \text{O}_2/(\text{Ar} + \text{O}_2)$] were applied during the sputtering process to optimize the electrical and optical properties of the r-ICO electrode. The optimized value of $r(\text{O}_2)$ was 0.13%, obtained by controlling the flow rates of the pure Ar and O₂/Ar mixture at 26 and 4 sccm, respectively.

Deposition of the Front ICO Electrode: A target material comprising 97 wt% In₂O₃ and 3 wt% CeO₂ was used to prepare the ICO front electrode (f-ICO). The f-ICO electrode was deposited on top of Corning glass. Prior to use, the glass substrates were cleaned sequentially with ammonia, hydrogen peroxide, deionized water, methanol, and isopropanol and then treated with oxygen plasma for 15 min to remove organic residues from the surface. The samples were transferred into the chamber of a sputtering machine; the chamber was evacuated until the pressure was less than 2×10^{-6} torr to eliminate excess oxygen and moisture. Pure Ar was used as the processing gas (flow rate: 35 sccm). The ICO front electrode was then deposited through RF sputtering (Kao Duen Tec. Co.) with a sputter power of 240 W under a working pressure of 3 mtorr. The deposition rate of the ICO front electrode was $\approx 0.11 \text{ nm s}^{-1}$. After deposition, the samples were transferred to a tubular furnace and annealed under vacuum at 300 °C for 30 min with a heating rate of 5 °C min⁻¹.

Fabrication of Opaque and ST-PVSCs: f-FTO glass (or f-ICO glass) was washed ultrasonically sequentially with acetone, methanol, and isopropanol. The NiO_x NP HTL layer (20 mg mL⁻¹ in deionized water) was spin coated onto clean FTO (or f-ICO) glass at 2500 rpm for 60 s and then annealed at 160 °C for 30 min in air. The NiO_x NPs were synthesized according to a previously published procedure.^[50] A 1.2 M solution of the perovskite precursor was prepared by mixing MAI and PbI₂ (1:1 molar ratio) in DMF and DMSO (5:2, v/v; 1 mL). This solution was spin coated onto the as-prepared NiO_x film at 4500 rpm for 30 s in a glove box filled with N₂. After spinning for 15 s, diethyl ether (300 μL) was added to the sample to wash out the extra solvent and form a transparent intermediate perovskite phase. All samples were then annealed on a hot plate—at 70 °C for 1 min and then at 100 °C for 2 min—to form dark-brown perovskite films. A PC₆₁BM solution (2.5 wt% in CB) was spin coated onto the perovskite layer at 1000 rpm for 30 s. Finally, the TBAOH–SnO₂ buffer layer was spin coated onto the PC₆₁BM layer at 1500 rpm for 30 s. To prepare the opaque device, a 100 nm-thick Ag rear electrode was deposited through thermal evaporation onto PCBM/TBAOH–SnO₂ with area of 0.09 cm². To prepare the semitransparent device, the r-ICO (or r-ITO) electrode was deposited onto the ETL with an area of 0.09 cm² through DC sputtering, as described earlier. Note that the ST-PVSC filter was made on a 2.5 × 2.5 cm² substrate with full coverage of the TE.

Fabrication and Measurement of 4T Perovskite/silicon Tandem Solar Cells: The PCEs of individual Si SCs and the ST-PVSCs were measured over an aperture area of 4 and 0.09 cm², respectively. For the PCE measurements of 4T perovskite/silicon tandem solar cells, we placed a 2.5 cm × 2.5 cm perovskite optical filter with the same ST-PVSC architecture on top of the Si SC. After covering with the perovskite optical filter, the filtered silicon bottom cell was measured over an aperture area of 4 cm². Measurements were performed using a voltage source meter (Keithley 2410) under an AM 1.5G solar simulator (Yamashita Denso) with irradiation at 100 mW cm⁻². The detail of the measurement procedure is presented graphically, as shown in Figure S10, Supporting Information. The PCEs of the 4T perovskite/Si tandem solar cells were calculated by adding together the PCEs of the perovskite top cell and the filtered silicon bottom cell. In this study, a

HJT Si SC was used as the bottom cell, supplied by United Renewable Energy Co., LTD. Taiwan.

Electronic Modeling of the Device: The drift-diffusion model was applied to quantitatively simulate the PVSCs. It describes the generation, transport, and recombination processes, using the following continuous equations for electrons and holes.

$$\frac{\partial n}{\partial t} = G - R + \frac{1}{q} \nabla \cdot J_n, \quad \frac{\partial p}{\partial t} = G - R - \frac{1}{q} \nabla \cdot J_p \quad (2)$$

where n and p are the electron and hole densities, respectively; G is a light-dependent generation rate of charge carriers; R represents all the recombination processes (Shockley–Read–Hall, modified Langevin and Auger models); q is the elementary charge constant; and J_n and J_p are the electron and hole drift-diffusion currents, respectively. The continuous equations were connected with the spatial electric field Poisson equation.

$$\nabla \cdot F = \frac{q}{\epsilon_0 \epsilon_r} (p - n + N_D - N_A) \quad (3)$$

where F is spatial electric field distribution, ϵ_0 is the vacuum permittivity constant, ϵ_r represents the permittivity of the layer, and N_D and N_A represent donor and acceptor concentrations in ETL and HTL, respectively. The model was discretized using the Scharfetter–Gummel method together with Chebyshev polynomials to apply a nonlinear spatial grid. To simulate the J – V characteristics, the model was solved by forward iteration in time to find the steady-state current for each applied voltage. To avoid neglecting the transportation losses due to energy differences between layers, the generalized potential method was applied. Further details of the model have been reported previously.^[51]

Characterization of Materials and Devices: The WF of the films were measured using UPS (PHI 5000 VersaProbe, ULVAC-PHI) with an ultraviolet light source of He I emission (21.2 eV, B50 W) and calculated using the equation

$$\Phi = h\nu - (E_0 - E_F) \quad (4)$$

XPS spectra were recorded using a PHI 5000 Versa Probe system (ULVAC-PHI, Chigasaki) and a microfocused (100 μm, 25 W) Al X-ray beam. The transmission (T) and reflection (R) spectra of TCO films and ST-PVSCs were measured using UV–vis–NIR spectroscopy (JASCO, V-770). The measurements were performed in the range 300–1200 nm with a step of 1 nm. The absorbances (A) of the films or ST-PVSCs were calculated using the equation

$$A = 100 - T - R \quad (5)$$

The free carrier densities and carrier mobilities of the TEs were determined through Hall effect measurements (ECOPIA, HMS-3000). Top-view and cross-sectional images of the devices were recorded using SEM (JEOL, JSM 7610FPLUS). The crystal structures of the f-ICO films were determined through XRD (Rigaku, TTRAX III) with Cu K α ($\lambda = 0.154 \text{ nm}$) radiation at 18 kV and over the range 15–65°. The J – V curves of devices having an active area of 0.09 cm² were measured through both forward (from –0.2 to +1.2 V) and backward (from +1.2 to –0.2 V) scans. The step voltage of the test and the delay time were 50 mV and 10 ms, respectively. Measurements were performed using a voltage source meter (Keithley 2410) under an AM 1.5 G solar simulator (Yamashita Denso) with irradiation at 100 mW cm⁻². ND filters were used to achieve lower light intensity. All of the devices were measured in air. The HJT c-Si solar cell having a size of 2 × 2 cm² was provided by United Renewable Energy (Taiwan). For the J – V measurements of the 4T-perovskite/silicon tandem solar cell, a 2.5 × 2.5 cm² ST-PVSCs filter was stacked on top of the HJT c-Si cell for measurement of the efficiency of the silicon bottom cell. The EQE spectra of the solar cell were measured using an EQE measurement system (Enlitech Taiwan, QE-R3011). Prior to measurement, the EQE system was calibrated using a silicon and germanium diode. The HJT c-Si solar cell was filtered by a 2.5 × 2.5 cm² ST-PVSC filter during EQE measurement.

Supporting Information

Supporting Information is available from the Wiley Online Library or from the author.

Acknowledgements

This study was supported financially by the Ministry of Science and Technology of Taiwan (MOST 109-3116-F-002-001-CC2; 108-2119-M-002-005; 110-2221-E-131-010), United Renewable Energy Co., LTD, Taiwan, and E-Sun Precision Industrial Co., LTD, Taiwan. Calculations were performed at the Academic Computer Centre (CI TASK) in Gdansk, Poland.

Conflict of Interest

The authors declare no conflict of interest.

Author Contributions

W.-F.S. and Y.-C.H. took care of conceptualization. W.-F.S. and P.-H.L. took care of methodology. P.-H.L. oversaw validation. Formal analysis was conducted by P.-H.L. Device fabrication and materials preparation were taken care of by P.-H.L. and T.-T.W. D.G. C.-F.L. and Y.-X.H. and S.-H.H. contributed to investigation. W.-F.S. and Y.-C.H. took care of resources. P.-H.L. contributed to visualization. Writing the original draft was carried out by P.-H.L. and W.-F.S. W.-F.S. and Y.-C.H. oversaw supervision. Writing, review, and editing were taken care of by Y.-C.H. and W.-F.S. Project administration was conducted by W.-F.S. and Y.-C.H.

Data Availability Statement

Research data are not shared.

Keywords

conducting oxides, near infrared, perovskites, semitransparent solar cells, silicon, tandem, transmission

Received: November 1, 2021

Revised: December 27, 2021

Published online:

- [1] National Renewable Energy Laboratory, *Best Research-Cell Efficiencies*, http://www.nrel.gov/pv/assets/images/efficiency_chart.jpg (accessed: November 2021).
- [2] K. Yamamoto, K. Yoshikawa, H. Uzu, D. Adachi, *Jpn. J. Appl. Phys.* **2018**, *57*, 08RB20.
- [3] L. C. Hirst, N. J. Ekins-Daukes, *Prog. Photovolt: Res. Appl.* **2011**, *19*, 286.
- [4] W. Shockley, H. J. Queisser, *J. Appl. Phys.* **1961**, *32*, 510.
- [5] M. I. Hossain, W. Qarony, S. Ma, L. Zeng, D. Knipp, Y. H. Tsang, *Nano-Micro Lett.* **2019**, *11*, 58.
- [6] A. D. Vos, *J. Phys. D: Appl. Phys.* **1980**, *13*, 839.
- [7] M. A. Green, A. Ho-Baillie, H. J. Snaith, *Nat. Photonics* **2014**, *8*, 506.
- [8] P. Gao, M. Grätzel, M. K. Nazeeruddin, *Energy Environ. Sci.* **2014**, *7*, 2448.
- [9] H. S. Jung, N.-G. Park, *Small* **2015**, *11*, 10.
- [10] Z. Li, M. Yang, J.-S. Park, S.-H. Wei, J. J. Berry, K. Zhu, *Chem. Mater.* **2016**, *28*, 284.
- [11] S. Kazim, M. K. Nazeeruddin, M. Grätzel, S. Ahmad, *Angew. Chem., Int. Ed.* **2014**, *53*, 2812.
- [12] C. D. Bailie, M. G. Christoforo, J. P. Mailoa, A. R. Bowering, E. L. Unger, W. H. Nguyen, J. Burschka, N. Pellet, J. Z. Lee, M. Grätzel, R. Noufi, T. Buonassisi, A. Salleo, M. D. McGehee, *Energy Environ. Sci.* **2015**, *8*, 956.
- [13] J. P. Mailoa, C. D. Bailie, E. C. Johlin, E. T. Hoke, A. J. Akey, W. H. Nguyen, M. D. McGehee, T. Buonassisi, *Appl. Phys. Lett.* **2015**, *106*, 121105.
- [14] H. H. Park, J. Kim, G. Kim, H. Jung, S. Kim, C. S. Moon, S. J. Lee, S. S. Shin, X. Hao, J. S. Yun, M. A. Green, A. W. Y. Ho-Baillie, N. J. Jeon, T.-Y. Yang, J. Seo, *Small Methods* **2020**, *4*, 2000074.
- [15] A. Al-Ashouri, E. Köhnen, B. Li, A. Magomedov, H. Hempel, P. Caprioglio, A. Márquez José, B. Morales Vilches Anna, E. Kasparavicius, A. Smith Joel, N. Phung, D. Menzel, M. Grischek, L. Kegelmann, D. Skroblin, C. Gollwitzer, T. Malinauskas, M. Jošt, G. Matič, B. Rech, R. Schlattmann, M. Topič, L. Korte, A. Abate, B. Stannowski, D. Neher, M. Stollerfoht, T. Unold, V. Getautis, S. Albrecht, *Science* **2020**, *370*, 1300.
- [16] F. Sahli, J. Werner, B. A. Kamino, M. Bräuninger, R. Monnard, B. Paviet-Salomon, L. Barraud, L. Ding, J. J. Diaz Leon, D. Sacchetto, G. Cattaneo, M. Despeisse, M. Boccard, S. Nicolay, Q. Jeangros, B. Niesen, C. Ballif, *Nat. Mater.* **2018**, *17*, 820.
- [17] B. Chen, Z. J. Yu, S. Manzoor, S. Wang, W. Weigand, Z. Yu, G. Yang, Z. Ni, X. Dai, Z. C. Holman, J. Huang, *Joule* **2020**, *4*, 850.
- [18] M. H. Futscher, B. Ehrler, *ACS Energy Lett.* **2016**, *1*, 863.
- [19] E. Della Gaspera, Y. Peng, Q. Hou, L. Spiccia, U. Bach, J. J. Jasieniak, Y.-B. Cheng, *Nano Energy* **2015**, *13*, 249.
- [20] B. Chen, Y. Bai, Z. Yu, T. Li, X. Zheng, Q. Dong, L. Shen, M. Boccard, A. Gruverman, Z. Holman, J. Huang, *Adv. Energy Mater.* **2016**, *6*, 1601128.
- [21] F. Guo, H. Azimi, Y. Hou, T. Przybilla, M. Hu, C. Bronnbauer, S. Langner, E. Spiecker, K. Forberich, C. J. Brabec, *Nanoscale* **2015**, *7*, 1642.
- [22] E. Lee, J. Ahn, H.-C. Kwon, S. Ma, K. Kim, S. Yun, J. Moon, *Adv. Energy Mater.* **2018**, *8*, 1702182.
- [23] Z. Li, S. A. Kulkarni, P. P. Boix, E. Shi, A. Cao, K. Fu, S. K. Batabyal, J. Zhang, Q. Xiong, L. H. Wong, N. Mathews, S. G. Mhaisalkar, *ACS Nano* **2014**, *8*, 6797.
- [24] J. Yoon, U. Kim, Y. Yoo, J. Byeon, S.-K. Lee, J.-S. Nam, K. Kim, Q. Zhang, E. I. Kauppinen, S. Maruyama, P. Lee, I. Jeon, *Adv. Sci.* **2021**, *8*, 2004092.
- [25] L. Bu, Z. Liu, M. Zhang, W. Li, A. Zhu, F. Cai, Z. Zhao, Y. Zhou, *ACS Appl. Mater. Interfaces* **2015**, *7*, 17776.
- [26] G. D. Spyropoulos, C. O. Ramirez Quiroz, M. Salvador, Y. Hou, N. Gasparini, P. Schweizer, J. Adams, P. Kubis, N. Li, E. Spiecker, T. Ameri, H.-J. Egelhaaf, C. J. Brabec, *Energy Environ. Sci.* **2016**, *9*, 2302.
- [27] K. A. Bush, C. D. Bailie, Y. Chen, A. R. Bowering, W. Wang, W. Ma, T. Leijtens, F. Moghadam, M. D. McGehee, *Adv. Mater.* **2016**, *28*, 3937.
- [28] J. Werner, G. Dubuis, A. Walter, P. Löper, S.-J. Moon, S. Nicolay, M. Morales-Masis, S. De Wolf, B. Niesen, C. Ballif, *Sol. Energy Mater. Sol. Cells* **2015**, *141*, 407.
- [29] E. Aydin, M. De Bastiani, X. Yang, M. Sajjad, F. Aljamaan, Y. Smirnov, M. N. Hedhili, W. Liu, T. G. Allen, L. Xu, E. Van Kerschaver, M. Morales-Masis, U. Schwingenschlögl, S. De Wolf, *Adv. Funct. Mater.* **2019**, *29*, 1901741.
- [30] G. Nogay, F. Sahli, J. Werner, R. Monnard, M. Boccard, M. Despeisse, F. J. Haug, Q. Jeangros, A. Ingenito, C. Ballif, *ACS Energy Lett.* **2019**, *4*, 844.

- [31] A. F. Palmstrom, J. A. Raiford, R. Prasanna, K. A. Bush, M. Sponseller, R. Cheacharoen, M. C. Minichetti, D. S. Bergsman, T. Leijtens, H.-P. Wang, V. Bulović, M. D. McGehee, S. F. Bent, *Adv. Energy Mater.* **2018**, *8*, 1800591.
- [32] M. Jošt, E. Köhnen, A. B. Morales-Vilches, B. Lipovšek, K. Jäger, B. Macco, A. Al-Ashouri, J. Krč, L. Korte, B. Rech, R. Schlatmann, M. Topič, B. Stannowski, S. Albrecht, *Energy Environ. Sci.* **2018**, *11*, 3511.
- [33] B. Chen, Z. Yu, K. Liu, X. Zheng, Y. Liu, J. Shi, D. Spronk, P. N. Rudd, Z. Holman, J. Huang, *Joule* **2019**, *3*, 177.
- [34] D. H. Kim, C. P. Muzzillo, J. Tong, A. F. Palmstrom, B. W. Larson, C. Choi, S. P. Harvey, S. Glynn, J. B. Whitaker, F. Zhang, Z. Li, H. Lu, M. F. A. M. van Hest, J. J. Berry, L. M. Mansfield, Y. Huang, Y. Yan, K. Zhu, *Joule* **2019**, *3*, 1734.
- [35] S. C. Baker-Finch, K. R. McIntosh, D. Yan, K. C. Fong, T. C. Kho, *J. Appl. Phys.* **2014**, *116*, 063106.
- [36] M. Morales-Masis, S. De Wolf, R. Woods-Robinson, J. W. Ager, C. Ballif, *Adv. Electron. Mater.* **2017**, *3*, 1600529.
- [37] Z. Ying, Y. Zhu, X. Feng, J. Xiu, R. Zhang, X. Ma, Y. Deng, H. Pan, Z. He, *Adv. Mater. Interfaces* **2021**, *8*, 2001604.
- [38] Y. Jiang, T. Feurer, R. Carron, G. T. Sevilla, T. Moser, S. Pisoni, R. Erni, M. D. Rossell, M. Ochoa, R. Hertwig, A. N. Tiwari, F. Fu, *ACS Nano* **2020**, *14*, 7502.
- [39] G. C. E. Jost, A. N. Hamri, F. Köhler, J. Hüpkes, *Phys. Status Solidi (A)* **2016**, *213*, 1751.
- [40] E. Kobayashi, Y. Watabe, T. Yamamoto, Y. Yamada, *Sol. Energy Mater. Sol. Cells* **2016**, *149*, 75.
- [41] K.-C. Hsiao, M.-H. Jao, K.-Y. Tian, T.-H. Lin, D.-P. Tran, H.-C. Liao, C.-H. Hou, J.-J. Shyue, M.-C. Wu, W.-F. Su, *Solar RRL* **2020**, *4*, 2000197.
- [42] P.-H. Lee, T.-T. Wu, K.-Y. Tian, C.-F. Li, C.-H. Hou, J.-J. Shyue, C.-F. Lu, Y.-C. Huang, W.-F. Su, *ACS Appl. Mater. Interfaces* **2020**, *12*, 45936.
- [43] D. L. Smith, D. W. Hoffman, *Phys. Today* **1996**, *49*, 60.
- [44] G. J. Exarhos, X.-D. Zhou, *Thin Solid Films* **2007**, *515*, 7025.
- [45] S. Deshpande, S. Patil, S. V. N. T. Kuchibhatla, S. Seal, *Appl. Phys. Lett.* **2005**, *87*, 133113.
- [46] W.-F. Wu, B.-S. Chiou, *Semicond. Sci. Technol.* **1996**, *11*, 196.
- [47] Y. S. Rim, D. L. Kim, W. H. Jeong, H. J. Kim, *Appl. Phys. Lett.* **2010**, *97*, 233502.
- [48] A. Sahai, N. Goswami, *Ceram. Int.* **2014**, *40*, 14569.
- [49] J. Zhang, J. Lu, Q. Jiang, B. Lu, X. Pan, L. Chen, Z. Ye, X. Li, P. Guo, N. Zhou, *J. Vac. Sci. Technol. B* **2014**, *32*, 010602.
- [50] P.-H. Lee, T.-T. Wu, C.-F. Li, D. Głowienka, Y.-H. Sun, Y.-T. Lin, H.-W. Yen, C.-G. Huang, Y. Galagan, Y.-C. Huang, W.-F. Su, *Chem. Eng. J.* **2021**, 412.
- [51] D. Głowienka, D. Zhang, F. Di Giacomo, M. Najafi, S. Veenstra, J. Szmytkowski, Y. Galagan, *Nano Energy* **2020**, *67*, 104186.